Journal of Power Sources 396 (2018) 246–256

Contents lists available at ScienceDirect

Journal of Power Sources

journal homepage: www.elsevier.com/locate/jpowsour

A novel approach for the quantification of inhomogeneous 3D current distribution in fuel cell electrodes

A. Bertei[a,b,*], V. Yufit[a], F. Tariq[a], N.P. Brandon[a]

[a] Department of Earth Science and Engineering, Imperial College London, SW7 2AZ, UK
[b] Department of Civil and Industrial Engineering, University of Pisa, 56122, Italy

HIGHLIGHTS

- Proposed particle-based method to quantify the 3D current distribution in electrodes.
- Current distribution at particle level is scattered within porous microstructures.
- 30% of electrode volume is underutilized as particles do not transfer enough current.
- Safe operation and advanced microstructural design can be based on this 3D method.
- This novel 3D methodology overcomes the limitations of macrohomogeneous modeling.

GRAPHICAL ABSTRACT

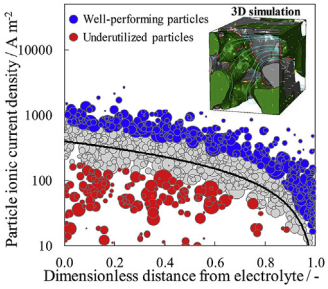

ARTICLE INFO

Keywords:
Modeling
3D tomography
Advanced characterization
Particle-based
Guidelines

ABSTRACT

The electrode microstructural properties significantly influence the efficiency and durability of many electrochemical devices including solid oxide fuel cells. Despite the possibility of simulating the electrochemical phenomena within real three-dimensional microstructures, the potential of such 3D microstructural information has not yet been fully exploited. We introduce here a completely new methodology for the advanced characterization of inhomogeneous current distribution based on a statistical analysis of the current of each particle within the microstructure. We quantify the large variation in local current distribution and link it to the particle size dispersion, indicating how particle coarsening can trigger further degradation. We identify two classes of particles: those transferring more current than average, which show 10–40% more particle-particle contacts, and those producing more current than average, characterized by ~2.5 times larger three-phase boundary length per unit volume. These two classes of particles are mutually exclusive, which implies that up to the 30% of the electrode volume within the functional layer is underutilized. This fundamental insight goes well beyond the predictions of continuum modeling, allowing us to revisit the current standards regarding safe operating conditions and to suggest alternative strategies based on nanoparticle infiltration, template-assisted synthesis and additive manufacturing for designing more durable electrodes.

1. Introduction

The twenty-first century is expected to witness the transition from the abundant use of fossil fuels to a clean and sustainable energy economy based on renewable resources [1]. In this scenario, electrochemical energy conversion and storage, as provided by fuel cells and

* Corresponding author. Department of Civil and Industrial Engineering, University of Pisa, 56122, Italy.
E-mail address: antonio.bertei@unipi.it (A. Bertei).

https://doi.org/10.1016/j.jpowsour.2018.06.029
Received 6 March 2018; Received in revised form 25 May 2018; Accepted 6 June 2018
Available online 14 June 2018

batteries, will play a prominent role [2,3]. Both these key technologies generally employ porous electrodes, typically consisting of a dispersion of granular particles or agglomerates, to extend the electrochemical reaction into a larger volume and thus decrease the internal losses of the energy conversion processes [4].

It has been widely recognized that the electrode microstructural characteristics significantly affect the electrochemical efficiency and durability of both fuel cells and batteries [5–9]. This has been widely investigated in the literature especially for solid oxide fuel cells (SOFCs) [10,11], which are chosen as the main focus of this study. Traditionally, the electrochemical behavior of the electrodes has been interpreted using macro-homogeneous models [12–16], which describe the conservation and transport of charged and chemical species in 1D or 2D by assimilating the porous microstructure to a homogeneous continuum, with averaged microstructural properties represented by effective transport and geometrical parameters [17,18]. Such effective microstructural properties were estimated only by using percolation models [19,20] until 3D tomography enabled the reconstruction of the real electrode microstructure [21–25].

However, despite the availability of the full structural details across different length scales, microstructural analysis has to date been still largely limited to obtaining averaged parameters, which characterize the electrode structure as a whole. Some examples include the tortuosity factor [21,26,27], which is a measure of how convoluted the conduction and diffusion pathways are, or the three-phase boundary (TPB) density [28,29], which is the length per unit volume of the contact perimeter among different conducting phases where charge-transfer occurs. In this way, complex 3D information is reduced to a single averaged value to simplify modeling. While simulating the transport and reaction processes within the reconstructed 3D microstructure has become computationally affordable [30–42], the full potential of such a three-dimensional electrochemical simulation has not yet been totally exploited. For example, 3D electrochemical simulation has been used to predict voltage profiles along the electrode thickness or polarization curves, which can be done with high fidelity by continuum models too [43–47]. However, 3D electrochemical simulation can be used to go beyond the predictions of macro-homogeneous models and to quantify the heterogeneous distribution of electrochemical processes [48,49], assessing the occurrence of hot spots or unbalanced current distribution which may trigger degradation phenomena [38,39], so that to identify their primary causes in order to guide the rational design of the electrode microstructure. Notably, at the present no experimental technique is capable to probe such three-dimensional inhomogeneous current distribution, thus modeling represents the only strategy currently available to provide this type of advanced guidelines. To the best of our knowledge, to date there are no published studies regarding the three-dimensional quantification of inhomogeneous current distribution and its implications on performance optimization and degradation. Such an improved understanding can be achieved by resolving the conducting phases into individual particles and characterizing the current distribution at the micro/nanoscopic particle level.

In this paper we propose a completely new methodology for the advanced microstructural characterization at the particle level, moving away from viewing the microstructure as a monolithic block, and explore its potential in both real and synthetic 3D electrodes, enabling identification of regions with specific properties relevant to performance as well as prediction and design of improved micro and nanostructures. As a case study to apply this methodology, we consider the functional layer of a porous SOFC anode made of Ni as the electron-conducting phase and scandia-stabilized zirconia (ScSZ) as the ion-conducting phase (see Fig. 1a). First, we mesh the digitally reconstructed phases (Fig. 1b) and solve for the transport and electrochemical reactions of charges and gas species within the 3D electrode microstructure, thus obtaining the electric potential, current density and gas concentration in every point of the corresponding phase (Fig. 1c). Then, the microstructure is resolved into individual particles (Fig. 1d and e), allowing for the quantification of the statistical distribution of current and other truly three-dimensional properties at the particle level. This approach enables exploitation of the full information contained in 3D microstructural datasets, enabling fundamental understanding of the reasoning behind inhomogeneous current and/or potential distributions, with their consequent impact on electrode lifetime, and suggesting strategies for the advanced design of porous electrodes.

2. Materials and methods

2.1. 3D tomography and generation of synthetic microstructures

The electrode under consideration is a porous SOFC anode made of Ni and ScSZ (solid volume fraction Ni/ScSZ equal to 40/60), operating at 973 K in 97% H_2–3% H_2O gas mixture [50,51], wherein the following electrochemical reaction:

$$H_{2(g)} + O^{2-}_{(ScSZ)} \rightarrow H_2O_{(g)} + 2e^{-}_{(Ni)} \quad (1)$$

is assumed to occur at the three-phase boundaries (TPBs) between the Ni, ScSZ and pore phase. The microstructure of this real electrode was reconstructed by using 3D tomography as described by Tariq et al. [52]. The electrode was impregnated with epoxy resin under vacuum to enhance the phase contrast during focused ion beam-SEM (FIB-SEM) tomography. A Ga-ion beam was used to mill a region of $\sim 2{\cdot}10^3\ \mu m^3$ for a total electrode thickness of 17 μm and thus acquire consecutive images with a voxel resolution of 30 nm. SEM images were aligned and segmented by using ImageJ [53] and Avizo 7.0.1 (Visualization Science Group, Mérignac, France). Fig. 1a shows a 3D rendering of the microstructure analyzed. The reconstructed domain can be viewed as the functional layer of a typical anode-supported SOFC. Notably, the functional layer is more relevant than the supporting layer in terms of 3D inhomogeneous current distribution because, in the functional layer, transport phenomena and electrochemical reactions interact each other. On the contrary, the supporting layer may be effectively described with a continuum approach [54].

Three synthetic microstructures were generated by using the packing algorithm described by Bertei et al. [55] and converted in voxel-basis by using isotropic voxels of 30 nm. The three synthetic structures consisted of a three-dimensional random arrangement of overlapping spherical particles within a box with square base of $12^2\ \mu m^2$ and thickness of 16.8 μm, nominally having the same porosity (~30%), Ni solid volume fraction (~40%) and mean particle diameter (~1.2 μm) of the tomographic dataset. The first synthetic structure, named “Synth 00”, was produced by using mono-dispersed particles while the other two structures, “Synth 20” and “Synth 40” respectively, were generated according to a Gaussian distribution of the particle diameter, centered at 1.2 μm, with a nominal standard deviation of 20% and 40%, respectively. A 3D rendering of the synthetic microstructures is shown in Fig. S1.

Both the real and synthetic microstructures were meshed in Simpleware ScanIP 7.0 (Synopsys, Mountain View, USA) to obtain conformal meshes of $\sim 40{\cdot}10^6$ elements.

2.2. Electrochemical modeling

The 3D numerical model, implemented in Comsol 5.2 [56] and reported in Table S1, is based on the conservation of electrons, oxygen ions and hydrogen within the corresponding phases, that is, Ni, ScSZ and pore phase, respectively. The physics and electrochemistry are kept as simple as possible to highlight only the effect of the 3D microstructure on the inhomogeneous current distribution. Within the bulk of each phase there is neither production nor consumption of charged or chemical species. The electronic and ionic current densities, I_e and I_O,

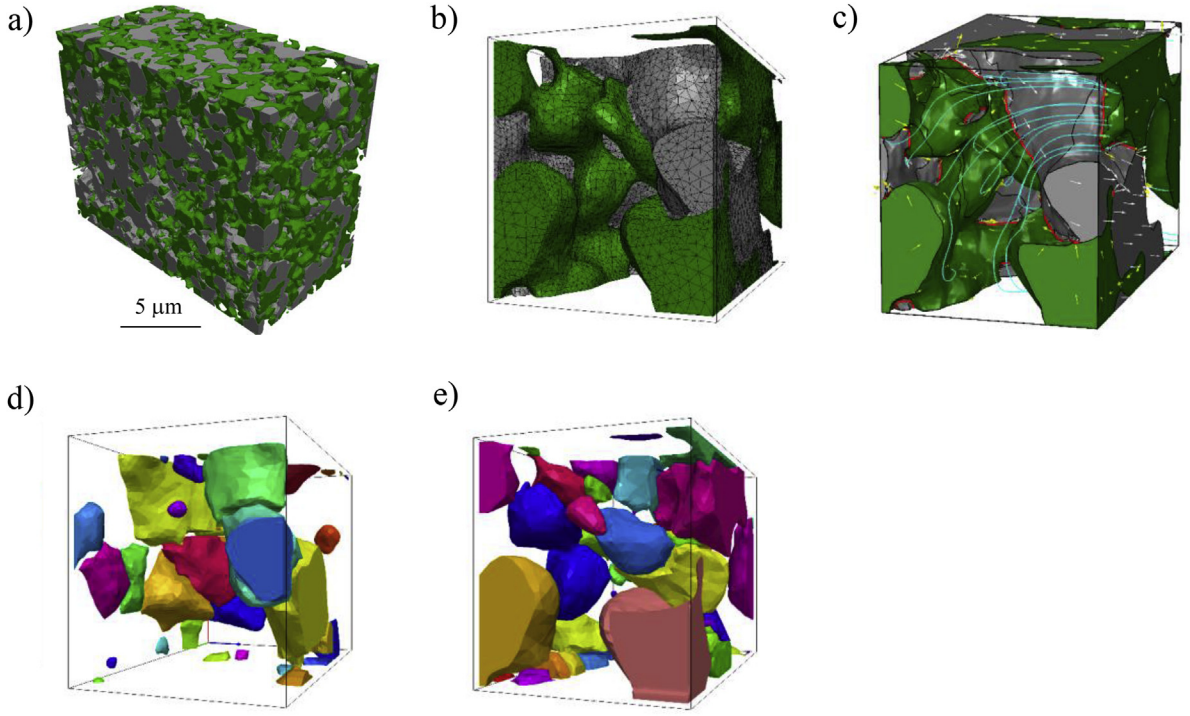

Fig. 1. Schematic illustration of the novel methodology for the advanced quantification of porous electrodes: a) 3D tomographic reconstruction of a real Ni/ScSZ porous anode (Ni in gray, ScSZ in green, pore phase is transparent); b) meshing and c) simulation of the electrochemical reaction at the TPB (in red) along with gas diffusion (in light blue) and electronic and ionic charge transport (gray and yellow arrows, respectively); d) identification of Ni and e) ScSZ particles according to watershed algorithm. Figures b–e refer to a small subset for visualization purposes. (For interpretation of the references to color in this figure legend, the reader is referred to the Web version of this article.)

are calculated according to Ohm law [57] by considering the electronic and ionic bulk conductivity of Ni and ScSZ, respectively. The molar flux of hydrogen N_H obeys the Fick law of diffusion, where the diffusion coefficient equals the binary diffusivity of the H_2/H_2O gas mixture.

The electrochemical reaction involving electrons, oxygen ions and hydrogen (Eq. (1)) is assumed to take place at each percolating three-phase boundary (TPB) among Ni, ScSZ and pores. The current exchanged per unit length of TPB, i_{TPB}, follows Butler-Volmer kinetics as a function of the local activation overpotential, η, which equals the difference between electronic and ionic potentials, V_{Ni} and V_{ScSZ}, and includes the local equilibrium potential difference [13,58]. i_{TPB} and η are considered positive in fuel cell operation mode.

The current exchanged at the TPB, i_{TPB}, represents a source term, applied along the TPB line, in the conservation equations of electrons, oxygen ions and hydrogen. In particular, i_{TPB} is linked to the current densities I_e and I_O and hydrogen flux N_H according to the reaction stoichiometry. This is mathematically enforced by integration in every infinitesimal control volume v shared by the three phases around an infinitesimal TPB line ℓ, as reported in Table S1, thus ensuring that the three conservation equations are coupled at the shared TPB.

The model is closed by boundary conditions. At the electrode/electrolyte interface, electronic current and hydrogen flux must vanish while the ScSZ ionic potential is set to zero as a reference potential. At the electrode/current collector interface, the ionic current is set to zero, the Ni electric potential is set equal to the total applied overpotential η_{tot} while the inlet hydrogen molar fraction is specified. No flux conditions are enforced elsewhere in every internal interface within the electrode domain.

A simple analytical solution of model equations is obtained by applying the macro-homogeneous approach, which assimilates the electrode microstructure to a continuum of the three phases with uniform effective properties [17]. Considering negligible electronic ohmic losses, fast gas diffusion and small activation overpotential, the profiles of ionic potential and current density along the electrode thickness are obtained analytically by solving for the conservation of oxygen ions. The analytical solution of such a 1D macro-homogeneous model is reported in Table S2 and is considered as a benchmark for the 3D simulation.

The list of symbols used in the model is reported in Table S3, while Table S4 and Table S5 summarize the parameters used in the 3D and 1D simulations, respectively. In particular, TauFactor [59] was used to evaluate the mean TPB density and the effective ionic conductivity required by the 1D analytical model.

2.3. Calculation of advanced microstructural metrics and integration with models

After solving the 3D model, the values of current density and electric potential are known at each node of the mesh. Numerical results are extracted by interpolating the values at the nodes of the mesh to a 3D grid with the same size of the original dataset. In parallel, the binary watershed algorithm implemented in Quiq3D (IQM Elements, London, UK) is used to resolve each phase of the segmented 3D microstructure into individual particles. Then, the two 3D datasets, containing particles and model solution, are superimposed: in this way, the mean value of current magnitude and electric potential can be associated to each particle. In addition, the contacts and TPB information are stored, thus enabling for the calculation of the current produced at the TPB of each particle. In order to make 3D particle statistics comparable to the analytical results of the 1D model, both the current density and the current produced per particle volume are normalized by multiplying for the volume fraction of the corresponding phase.

It is worth noting that the same particle-based statistical approach can be used regardless the specific electrochemistry simulated by the model; for example, the statistical analysis may concern the distribution of the degree of particle lithiation in lithium-batteries [60].

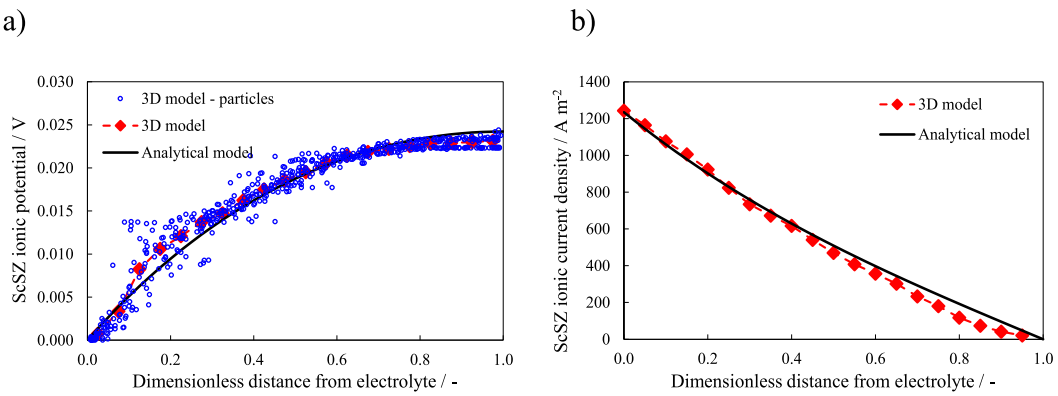

Fig. 2. Validation of the 3D numerical simulation against the prediction of the analytical macro-homogeneous model reported in Table S2: a) ScSZ ionic potential and b) ionic current density as a function of the dimensionless distance from the electrolyte. The prediction of the analytical model is reported with a black solid line while the red dashed line shows the results of the 3D model averaged within 20 cross sections parallel to the electrolyte interface. The blue circles in a) refer to the ionic potential of the individual ScSZ particles identified in the 3D model. (For interpretation of the references to color in this figure legend, the reader is referred to the Web version of this article.)

3. Results and discussion

3.1. Validation of the 3D simulation

Before extracting advanced metrics, the validity of the 3D numerical simulation must be assessed against the analytical predictions of the macro-homogeneous model described in Table S2. Such an analytical solution for the current and ionic potential distributions represents the benchmark of the state-of-the-art macro-homogeneous models used in the literature [17], which has been extensively validated with experimental data [51]. Fig. 2 shows the ionic potential and ionic current profiles along the thickness of the anode. The ionic potential increases while the ionic current density monotonously decreases along the thickness, indicating that the charge-transfer reaction is distributed over the whole electrode volume. The 3D model (red dashed line) quantitatively reproduces the same trends predicted by the analytical solution (black solid line). The ionic potential of individual ScSZ particles as obtained by the 3D model (blue circles) follows closely the analytical trend. The same considerations apply to the potential and current distributions obtained in three synthetic microstructures as reported in Fig. S2.

The smooth trends and the good match between analytical predictions and 3D model results indicate that the three-dimensional volume analyzed is big enough to be statistically representative of the entire electrode microstructure [39,61]. In addition, the characteristic active thickness t_δ [62–64], wherein most of the charge-transfer occurs, is in the order of 13 μm, which is much larger than the mean particle diameter (~1.2 μm); therefore, macroscopic gradients spread on a length scale much larger than particle size [54,65,66]. This implies that field variables, such as the electric potential and current density, are quite uniform within each particle, so that each particle can be completely characterized by a single value of potential and a single value of current density. This justifies the applicability of our novel approach, introduced in the next Section, which is based on the statistical analysis of the potential and current evaluated in each individual particle.

However, the uniformity of current and potential fields within each particle does not necessarily mean that, in any cross section parallel to the electrolyte, each particle experiences the same potential and current expected from the macro-homogeneous volume averaging: the scattering of the particle ionic potential in Fig. 2a points out that there is local heterogeneity of the microstructure. Hence, any deviations of particle current or particle potential from the expected mean value provide useful statistical information about the intrinsic heterogeneous, three-dimensional current distribution within the microstructure.

In summary, Fig. 2 demonstrates the soundness of the 3D numerical results. While the mean trends of current and potential can be easily predicted by continuum macro-homogeneous models as already reported in the literature [43–47], the statistical distribution of the deviations from the mean at the particle level contains truly three-dimensional information. The analysis, exploitation and significance of this information is discussed in the next Section.

3.2. Novel advanced microstructural analysis

As anticipated in the previous Section, the deviation of particle current density from the expected mean value contains useful information, which cannot be predicted by continuum macro-homogeneous models nor can it experimentally be measured by using the present electrochemical probes [67,68]. A statistical analysis of the current experienced by each particle is thus necessary to achieve a fundamental understanding of the impact of the three-dimensional microstructure on electrode performance.

Fig. 3a and b reports the distribution of the electronic and ionic current density within each Ni and ScSZ particle as a function of the distance from the electrolyte. Each particle is represented by a circle whose radius is proportional to the particle volume. The black solid line identifies the expected mean value of current density as predicted by the macro-homogeneous model. Particles showing a current density at least twice larger than the expected mean value are marked in blue, while particles with a current density smaller than half the expected value are marked in red. The vertical dot-dashed lines indicate the center coordinate of each distribution.

Fig. 3a and b shows that the particles current distribution is markedly scattered around the mean current profile. Such a wide scatter is present also in synthetic microstructures, as reported in Figs. S3–S5. Critically, this means that two particles, despite being at the same distance from the electrolyte and having similar volume, may experience completely different current densities. In other words, particles do not behave homogeneously and do not transfer the same current.

Such a wide scatter poses serious limitations to the application of macro-homogeneous models for the definition of safe operating conditions. For example, one may constrain the maximum operating current of the electrode in order to prevent excessive Joule heating [69], which may trigger degradation phenomena. However, Fig. 3a and b shows that the real maximum current density experienced by particles is significantly larger than the expected maximum value predicted by continuum models. In fact, the maximum current density predicted by the continuum analytical model is equal to 1235 $A\,m^{-2}$ in the simulated operating conditions; Fig. 3a and b reveals that there exist particles experiencing current density values beyond 4000 $A\,m^{-2}$, that is

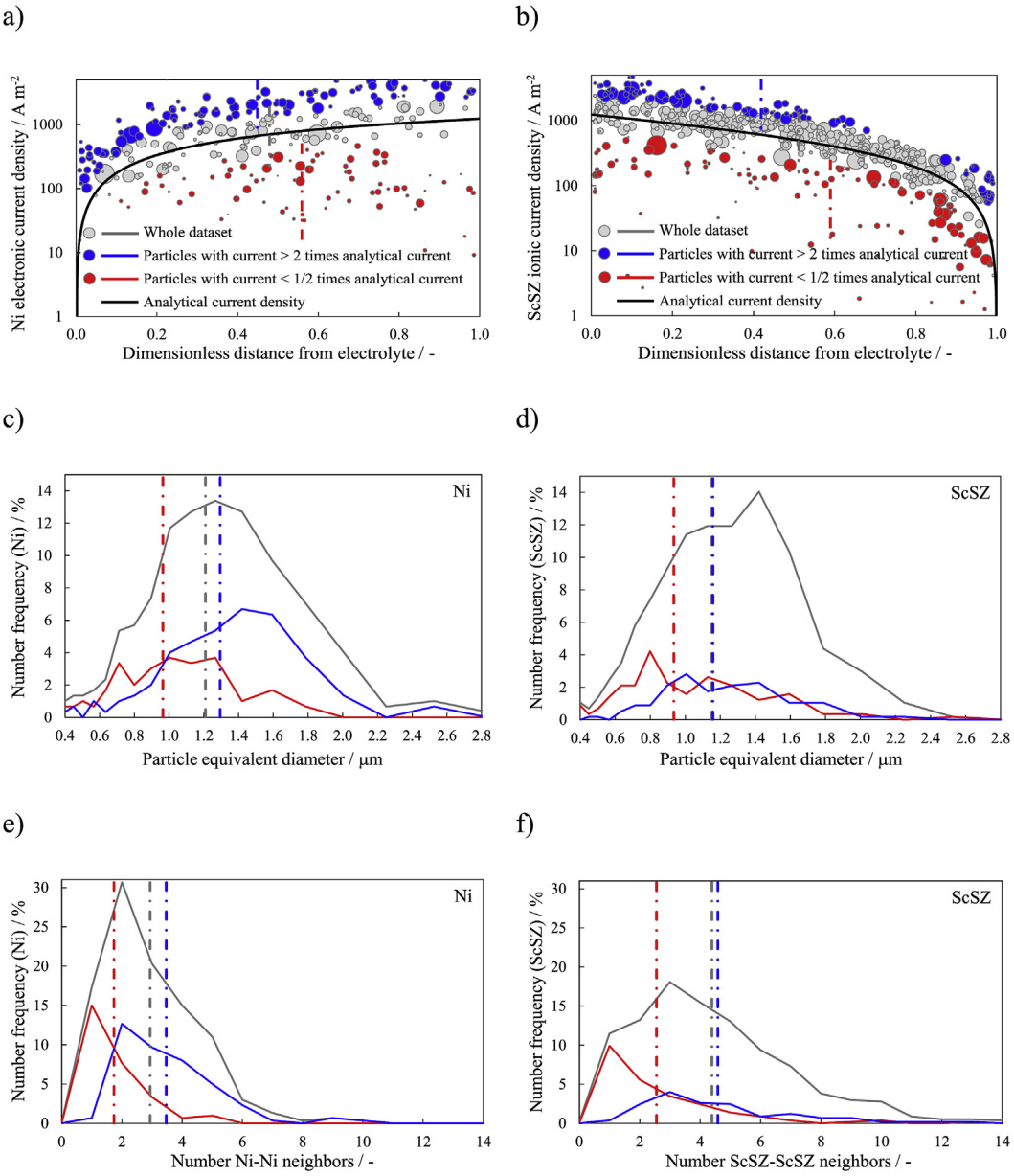

Fig. 3. Current density distribution at the particle level. a) Electronic current density for Ni particles and b) ionic current density for ScSZ particles as a function of the dimensionless distance from the electrolyte. The black solid line reports the mean current profile predicted by the analytical macro-homogeneous model. The radius of the bubble is proportional to particle volume. Note that the y-axis is plotted in logarithmic scale. c) Frequency distribution of the equivalent diameter of Ni and d) ScSZ particles. e) Frequency distribution of the number of neighbors per particle for Ni and d) ScSZ, where neighbors are particles of the same phase in contact with each other. The whole dataset is reported in gray, particles transferring at least twice the average current are reported in blue, while particles transferring less than half the average current are reported in red. The vertical dot-dashed lines refer to the center coordinate of each distribution. (For interpretation of the references to color in this figure legend, the reader is referred to the Web version of this article.)

more than three times larger than what predicted by continuum modeling. Such high current density values generate local Joule heating, as further elaborated in Fig. S12, which shows that up to 6% of ScSZ volume and 8% of Ni volume are subject to a local Joule heating larger than what continuum modeling predicts. Hence, continuum models underestimate the maximum current density experienced by particles at least by a factor 3, and as such are inapplicable for the determination of safe operating conditions, which can instead only be assessed by the truly three-dimensional approach that we have developed.

The reason why the particles current distribution is scattered around the mean value can be discovered through a statistical analysis at the particle level. Fig. 3c and d reports the particle size distribution for Ni and ScSZ for both the whole dataset (gray) as well as for the particles transferring at least twice the average current (blue) and less than half the average current (red). For the sake of conciseness, the last two classes of particles are denoted in the following as blue particles and red particles. Fig. 3c and d shows that red particles are predominantly small particles, being 10–20% smaller than average. On the other hand, blue particles are typically slightly larger than the mean diameter of the phase, although not necessarily. These results are confirmed in synthetic datasets (Figs. S3–S5), denoting generality of the behaviors found. However, the particle diameter is not an unambiguous microstructural descriptor to distinguish between blue and red particles.

A clearer insight is given by Fig. 3e and f, which reports the frequency distribution of the number of neighbors for each phase. In this study, two particles of the same phase are considered neighbors if they are in contact each other. Therefore, the number of neighbors identifies the connectivity of a particle within the phase it belongs to. Fig. 3e and

f shows that there is a clear separation between red and blue particles in terms of connectivity, with red particles having 40–50% less neighbors than average (mostly having just one neighbor, which prevents current to be transferred to another particle), while blue particles have at least two neighbors and, in general, 10–40% more neighbors than average. Notably, red particles account for up to 14% of ScSZ volume though all ScSZ particles are percolating. Figs. S3–S5 confirm these results in synthetic microstructures for both the Ni and ScSZ phases.

The advanced analysis reported in Fig. 3 enabled particle connectivity to be identified as the key reason why particles transfer less or more current than average. Irrespective of the phase considered, particles with 40–50% less neighbors than average transfer less current, while most of the current is carried by particles with at least two neighbors having 10–40% more neighbors than average. Particle connectivity is particularly important for the Ni phase (Fig. 3e), whose main function is to transfer electrons away from the electrode active region, which is close to the electrolyte interface.

A similar approach has been adopted for the analysis of the current per unit volume exchanged by particles at their three-phase boundaries. Notably, while Fig. 3 focused on the capability of particles to transfer current within the same phase, here the analysis addresses the efficacy of particles to exchange current from one phase to the other, which is related to the rate of the electrochemical reaction described in Eq. (1). Fig. 4a and b reports the current per unit of electrode volume produced within Ni and ScSZ particles as a function of the distance from the electrolyte. As in Fig. 3, particles are classified into those that produce at least twice the average current (blue) and less than half the average current (red). Figs. S6–S8 report the same results for three synthetic microstructures.

Fig. 4a and b shows that current production is not uniformly distributed among the particles, varying over more than two orders of magnitude through the electrode. The analysis of the particle size distribution in Fig. 4c and d reveals that blue particles are generally 15–30% smaller than average and constitute just a tiny fraction of the phase, being about 5% of the phase volume. On the other hand, a large fraction of particles, accounting for 20–30% of the solid volume within the functional layer, produce less current than average.

Fig. 4e and f shows that the TPB length per unit of particle volume is the key microstructural property to distinguish between red particles and blue particles. In fact, there is a clear separation between the two classes of particles: red particles have 50–90% less TPB density than average (or no TPB at all), while blue particles show about 2.5–3 times more TPB than average. This behavior is confirmed in the three synthetic microstructures (Figs. S6–S8).

The relevant outcomes of Figs. 3–4 are schematically summarized in Table 1, which reports the necessary conditions for a particle to transfer or produce more or less current than average. Generally, a large fraction of both solid phases is made up by particles which do not significantly contribute to the electrochemical reaction, only a tiny fraction of particles outperform the others. The size of the particles is not sufficient to distinguish well-performing from poor-performing particles, with small particles transferring less current than average while also producing more current per unit volume. Instead, other fundamental microstructural descriptors enable distinction between the two classes of particles: particle connectivity is relevant for transferring current within the same phase, while the current conversion between different phases is determined by the TPB length per unit of particle volume.

Thus, the intrinsic stochastic distributions of number of neighbors and TPB length per particle produce the broad scattering of the current profiles discussed in Figs. 3 and 4, resulting in a volume fraction up to 28% of particles which do not contribute significantly to current production, and just a tiny volumetric fraction, as low as 4%, which is more suited for current conversion by producing at least twice the average current but may also be responsible for localized Joule heating and, as a result, accelerated degradation. The next Section explores how electrode manufacturing can be efficiently informed to overcome these limitations by exploiting these new insights.

3.3. Strategies for advanced electrode design

The advanced microstructural characterization presented in the previous Section revealed inhomogeneous current distribution at the particle level and enabled identification of the key microstructural properties to enhance performance, namely particle connectivity and TPB length per unit of particle volume. The randomness of the particle arrangement [70] affects the distribution of such microstructural properties, causing inhomogeneous current transfer and, ultimately, an inefficient utilization of the electrode microstructure. Therefore, different strategies can be explored to optimize the electrode microstructure.

The first investigation concerns how the particle size dispersion affects the inhomogeneous current distribution. Three synthetic microstructures, consisting of randomly dispersed overlapping spherical particles, were generated as shown in Fig. S1. The synthetic microstructures have the same nominal macroscopic properties except for the standard deviation of the particle size dispersion, ranging from 0% (i.e., mono-dispersed particles) up to 40%. The advanced microstructural analysis of the synthetic structures is reported in Figs. S3–S8.

Fig. 5 summarizes the most relevant results regarding the solid volume fraction of particles producing less than half the average current (red particles, Fig. 5a) or more than twice the average (blue particles, Fig. 5b). Fig. 5a indicates that as the particle size dispersion increases, the fraction of particles which produce less current than average increases, being up to ~30% for ScSZ. This means that up to ~1/3 of the ionic conductor volume is underutilized in terms of current conversion. Consequently, a larger fraction of particles are forced to outperform producing more current than average (Fig. 5b), albeit representing only a minor fraction of the phase volume if compared with poor-performing particles. Therefore, we can conclude that a broader particle size dispersion produces a broader distribution of current produced per particle, that is, a more inhomogeneous current distribution. Moreover, as shown by Fig. S2b, the total current produced by the electrode decreases as the particle size dispersion increases.

These results suggest that a wide particle size dispersion may have detrimental effects on electrode performance, especially for its degradation. For example, inhomogeneous current production can generate high local steam partial pressure and high local heat flux, which may locally trigger Ni coarsening [71–77]. As Ni particles coarsen, the particle size dispersion increases [78,79], thus inducing further inhomogeneous current distribution according to our results. Furthermore, should Ni percolation be lost in some regions of the electrode, other regions will compensate at the expenses of larger local current densities, triggering further degradation processes, not only in the Ni phase but also in the ionic conductor since current conversion takes place at the shared TPBs. Although these implications can only be indicative at the present, the methodology we propose is capable of confirming these conclusions when coupled to *in-operando* 3D tomography of electrodes during degradation tests [80–83] or with experimental electrochemical probing [67,68], which is currently limited to 2D slices though.

A further insight to guide electrode manufacturing stems from a closer inspection of the results highlighted in Figs. 3–4 and in Table 1. In particular, we showed that two groups of particles can be identified: those transferring more current than average, characterized by a large number of neighbors, and those producing more current than average, characterized by a large TPB length per unit volume. Ideally, a particle is optimally utilized if it belongs to both groups, thereby excelling in both transferring and producing current. As a consequence, the optimal electrode microstructure should seek to maximize the fraction of such ideally utilized particles.

In Fig. 6a and b particles are plotted as a function of the number of

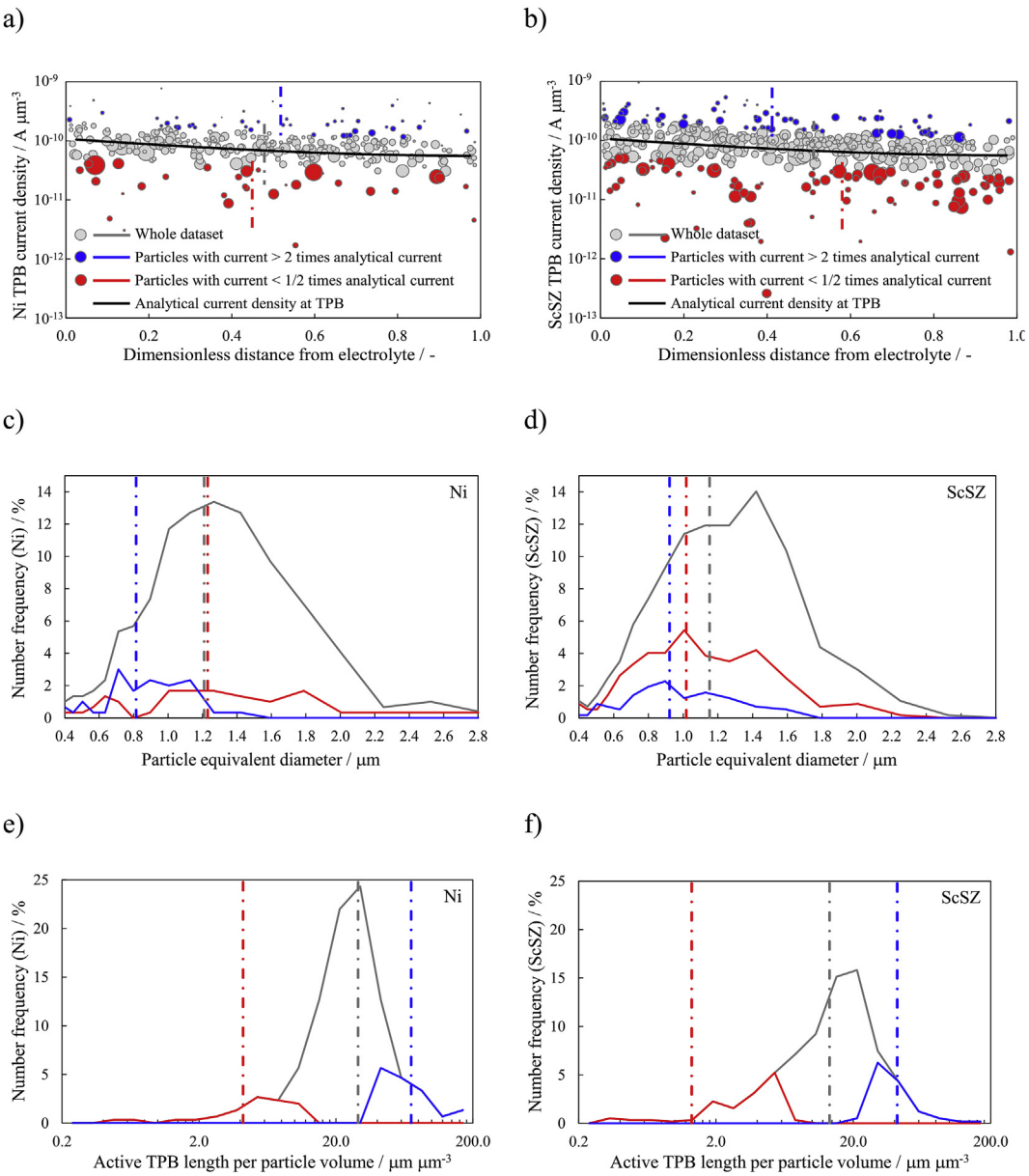

Fig. 4. Distribution of current produced at the TPB at the particle level. a) Current produced at the TPBs of particles per unit of electrode volume as a function of the dimensionless distance from the electrolyte for Ni particles and b) ScSZ particles. The black solid line reports the mean volumetric current profile predicted by the analytical macro-homogeneous model. The radius of the bubble is proportional to particle volume. Note that the y-axis is plotted in logarithmic scale. c) Frequency distribution of the equivalent diameter of Ni and d) ScSZ particles. e) Frequency distribution of the active TPB length per particle volume for Ni and f) ScSZ. The whole dataset is reported in gray, particles producing at least twice the average current are reported in blue, while particles producing less than half the average current are reported in red. The vertical dot-dashed lines refer to the center coordinate of each distribution. (For interpretation of the references to color in this figure legend, the reader is referred to the Web version of this article.)

neighbors and the TPB length per unit volume: particles transferring at least twice the average current are reported in purple, particles producing at least twice the average current are colored in blue, while particles belonging to both the groups are marked in green. Fig. 6a and b shows that the particles belonging to the first group (in purple) are gathered at the top-left corner of the graph, that is, in the region populated by particles with high connectivity, while particles belonging to the second group (in blue) lie in the bottom-right corner where the TPB length per unit volume is maximized. Particles which excel in both transferring and producing more current than average (in green) lie in

Table 1
Summary of necessary conditions for particles in order to transfer or produce more than twice or less than half the average current.

Particle class	Diameter		No. neighbors		TPB per particle volume	
	Current transfer	Current production	Current transfer	Current production	Current transfer	Current production
Less than half average current (red)	10–20% smaller	/	40–50% smaller	/	/	50–90% smaller
More than twice average current (blue)	/	15–30% smaller	10–40% larger	/	/	150% larger

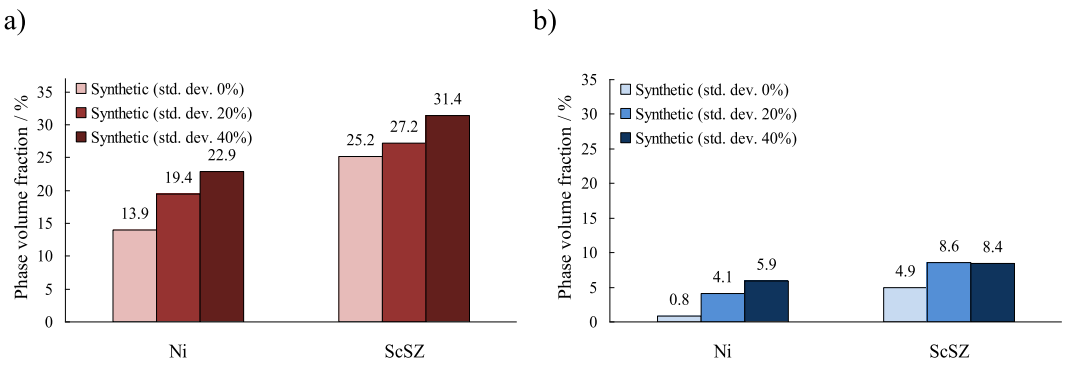

Fig. 5. Solid volume fraction of particles producing current at TPB a) less than half the average current, b) at least twice the average current, for three synthetic structures with different standard deviations of the particle size distribution.

the middle of the two groups. Notably, these ideally utilized particles constitute only a tiny fraction of the solid volume, as low as 1%. These trends are confirmed also in the synthetic structures as reported in Figs. S9–S11.

Fig. 6c schematically summarizes the results. Ideally, the fraction of (green) particles which transfer and produce more current than average should be increased in an optimized microstructure, which would imply that both the number of neighbors and the TPB length per particle should be increased simultaneously. However, Fig. 6 indicates that this ideal design paradigm is not achievable because having both a large number of neighbors with particles of the same phase and a large TPB length with particles of the other phase are mutually exclusive conditions. In other words, a particle cannot be in contact with both other particles of the same phase to transfer current and, simultaneously, with particles of the other phase to create an extended TPB to produce current. This intrinsic constraint poses fundamental limitations to the optimal exploitation of random electrode microstructures.

Therefore, an alternative strategy can be foreseen by designing electrodes with particles specifically arranged to fulfill two specific functions: a fraction of particles, organized to have a large number of neighbors (i.e., moving upward in Fig. 6c), in order to transfer current, and another fraction of particles, having large TPB length (i.e., moving rightward in Fig. 6c), to produce current. Hence, the practical design strategy suggests decoupling the two functions, to optimize specific classes of particles to fulfill each function individually rather than trying to arrange particles in a way to maximize both current transfer and current production.

This strategy sets the pathway for advanced manufacturing of electrodes. Scaffold electrodes infiltrated with nanoparticles [84–89] are an example of the adoption of such a strategy: the scaffold provides pathways for current transport while the dispersed nanoparticles provide large TPB length for current production. Additive manufacturing [90–92], once optimized, can go even beyond and fully implement the strategy we suggest. According to Fig. 6c, an advanced electrode microstructure should comprise a structured backbone for fast current transport along with lateral finer branches to boost current production, mimicking a fractal arrangement resembling for example human lungs (see inset in Fig. 6c). All the three phases (i.e., ion-conducting, electron-conducting and pore phase) should ideally be structured in this way, although the porous phase might be simply randomly dispersed in the case of fast gas transport. These indications complement the recent guidelines we established for the 3D manufacturing of porous electrodes [93] as well as the indications provided by macro-homogeneous modeling regarding microstructural optimization as a function of electrode thickness and operating conditions [17,18].

In summary, the fundamental understanding gained through our novel 3D characterization methodology revealed the fundamental limitations of random microstructures and sets a practical strategy to manufacture advanced electrodes with particles organized to maximize either current transport or current production, indicating that achieving both functions simultaneously by the same class of particles is not feasible.

4. Conclusions

This paper presented the potential of an innovative methodology to perform the advanced three-dimensional characterization at the particle level in porous electrodes. The methodology consists of simulating the transport and electrochemical reaction phenomena within the 3D microstructure of electrodes, and then performs a statistical analysis of the current experienced by each particle. Rather than focusing on average properties, which can be readily predicted by existing continuum models, this new methodology allowed us to focus on the distribution of electrochemical performance at the particle level and rationalize the reasoning behind the observed inhomogeneous current distribution.

Simulation results showed that the current at the particle level is significantly distributed around the mean, revealing that particles do not behave uniformly. Two classes of particles were identified, accomplishing specific functions: particles which transfer more current than average, characterized by 10–40% more contacts than average, and particles which produce more current than average, which show ~2.5 times more three-phase boundary length than average. These two classes are mutually exclusive each other, so that up to the 30% of electrode solid volume within the functional layer is shown to be underutilized.

The fundamental insight gained by this novel analysis allowed us to suggest specific strategies for the advanced manufacturing of electrodes, which should be oriented towards the design of microstructures with backbone particles for optimized current transport along with other particles conveniently arranged to maximize current production. On the other hand, conventional electrodes with random microstructures are limited by inherently inhomogeneous current distribution, which broadens as the particle size dispersion increases. This is expected to trigger local degradation mechanisms, revealing that safe operating conditions should be set on the basis of the 3D methodology that we propose, because continuum approximations will always underestimate the maximum local current density and Joule heating.

Although these behaviors were demonstrated in solid oxide fuel cell anodes, model equations can be easily adapted to take into account additional transport, reaction and surface phenomena as well as to apply the methodology to other electrochemical systems where porous electrodes are used, including batteries, fuel cells and electrolyzers.

Acknowledgements

This project has received funding from the European Union's Horizon 2020 research and innovation programme under the Marie

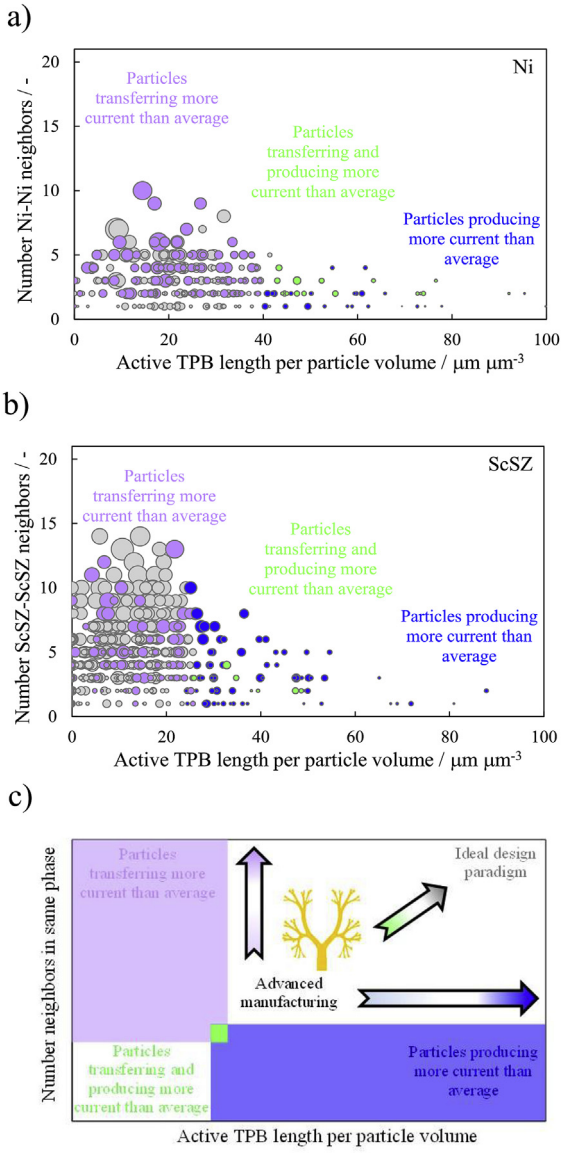

Fig. 6. Summary of the advanced statistics of current transfer and current production. a) Plot of the particles as a function of the number of neighbors (y-axis) and the active TPB length per unit of particle volume (x-axis) for Ni and b) ScSZ. The radius of the bubble is proportional to particle volume. Only well-performing particles are marked here: particles transferring at least twice the average current are indicated in purple, particles producing at least twice the average current are colored in blue. Particles belonging to both the two groups are marked in green. c) Schematic interpretation of the two graphs, indicating the direction for an ideal microstructural optimization, which is practically unfeasible because increasing simultaneously both neighbors and TPB length per particle are mutually exclusive conditions, and the suggested strategy proposed for advanced manufacturing. (For interpretation of the references to color in this figure legend, the reader is referred to the Web version of this article.)

Skłodowska-Curie grant agreement No 654915 and the EPSRC grants EP/M014045/1 and EP/M009521/1. The European project MARS-EV (FP7-NMP, No 609201) is also acknowledged. The Imperial College Research Computing Service (http://dx.doi.org/10.14469/hpc/2232) and especially its manager Dr. Matthew Harvey are gratefully acknowledged for providing access to the high-performing computing facilities at Imperial College London.

Appendix A. Supplementary data

Supplementary data related to this article can be found at http://dx.doi.org/10.1016/j.jpowsour.2018.06.029.

References

[1] J.D. Holladay, J. Hu, D.L. King, Y. Wang, An overview of hydrogen production technologies, Catal. Today 139 (2009) 244–260, http://dx.doi.org/10.1016/j.cattod.2008.08.039.
[2] M. Armand, J.M. Tarascon, Building better batteries, Nature 451 (2008) 652–657, http://dx.doi.org/10.1038/451652a.
[3] E.D. Wachsman, C.A. Marlowe, K.T. Lee, Role of solid oxidefuel cells in a balanced energy strategy, Energy Environ. Sci. 5 (2012) 5498–5509, http://dx.doi.org/10.1039/C1EE02445K.
[4] M. Winter, R.J. Brodd, What are batteries, fuel cells, and supercapacitors? Chem. Rev. 104 (2004) 4245–4269, http://dx.doi.org/10.1021/cr020730k.
[5] A. Atkinson, S. Barnett, R.J. Gorte, J.T.S. Irvine, A.J. McEvoy, M. Mogensen, S.C. Singhal, J. Vohs, Advanced anodes for high-temperature fuel cells, Nat. Mater. 3 (2004) 17–27, http://dx.doi.org/10.1038/nmat1040.
[6] H. Yokokawa, H. Tu, B. Iwanschitz, A. Mai, Fundamental mechanisms limiting solid oxide fuel cell durability, J. Power Sources 182 (2008) 400–412, http://dx.doi.org/10.1016/j.jpowsour.2008.02.016.
[7] M. Juhl, S. Primdahl, C. Manon, M. Mogensen, Performance/structure correlation for composite SOFC cathodes, J. Power Sources 61 (1996) 173–181, http://dx.doi.org/10.1016/S0378-7753(96)02361-0.
[8] J.R. Wilson, J.S. Cronin, S.A. Barnett, Linking the microstructure, performance and durability of Ni-yttria-stabilized zirconia solid oxide fuel cell anodes using three-dimensional focused ion beam-scanning electron microscopy imaging, Scripta Mater. 65 (2011) 67–72, http://dx.doi.org/10.1016/j.scriptamat.2010.09.025.
[9] L. Holzer, B. Münch, B. Iwanschitz, M. Cantoni, T. Hocker, T. Graule, Quantitative relationships between composition, particle size, triple phase boundary length and surface area in nickel-cermet anodes for solid oxide fuel cells, J. Power Sources 196 (2011) 7076–7089, http://dx.doi.org/10.1016/j.jpowsour.2010.08.006.
[10] Z. Gao, L.V. Mogni, E.C. Miller, J.G. Railsback, S.A. Barnett, A perspective on low-temperature solid oxide fuel cells, Energy Environ. Sci. 9 (2016) 1602–1644, http://dx.doi.org/10.1039/C5EE03858H.
[11] E.D. Wachsman, K.T. Lee, Lowering the temperature of solid oxide fuel cells, Science 334 (80) (2011) 935–939, http://dx.doi.org/10.1126/science.1204090.
[12] S.B. Adler, J.A. Lane, B.C.H. Steele, Electrode kinetics of porous mixed-conducting oxygen electrodes, J. Electrochem. Soc. 143 (1996) 3554–3564, http://dx.doi.org/10.1149/1.1837252.
[13] W.G. Bessler, S. Gewies, M. Vogler, A new framework for physically based modeling of solid oxide fuel cells, Electrochim. Acta 53 (2007) 1782–1800, http://dx.doi.org/10.1016/j.electacta.2007.08.030.
[14] H. Zhu, R.J. Kee, V.M. Janardhanan, O. Deutschmann, D.G. Goodwin, Modeling elementary heterogeneous chemistry and electrochemistry in solid-oxide fuel cells, J. Electrochem. Soc. 152 (2005) A2427–A2440, http://dx.doi.org/10.1149/1.2116607.
[15] J. Newman, W. Tiedemann, Porous-electrode theory with battery applications, AIChE J. 21 (1975) 25–41, http://dx.doi.org/10.1002/aic.690210103.
[16] M. Rahmanipour, A. Pappacena, M. Boaro, A. Donazzi, A distributed charge transfer model for IT-SOFCs based on ceria electrolytes, J. Electrochem. Soc. 164 (2017) F1249–F1264, http://dx.doi.org/10.1149/2.1911712jes.
[17] P. Costamagna, P. Costa, V. Antonucci, Micro-modelling of solid oxide fuel cell electrodes, Electrochim. Acta 43 (1998) 375–394, http://dx.doi.org/10.1016/S0013-4686(97)00063-7.
[18] A. Bertei, B. Nucci, C. Nicolella, Microstructural modeling for prediction of transport properties and electrochemical performance in SOFC composite electrodes, Chem. Eng. Sci. 101 (2013) 175–190, http://dx.doi.org/10.1016/j.ces.2013.06.032.
[19] D. Chen, Z. Lin, H. Zhu, R.J. Kee, Percolation theory to predict effective properties of solid oxide fuel-cell composite electrodes, J. Power Sources 191 (2009) 240–252, http://dx.doi.org/10.1016/j.jpowsour.2009.02.051.
[20] A. Bertei, C. Nicolella, Percolation theory in SOFC composite electrodes: effects of porosity and particle size distribution on effective properties, J. Power Sources 196 (2011) 9429–9436, http://dx.doi.org/10.1016/j.jpowsour.2011.06.087.
[21] J.R. Wilson, W. Kobsiriphat, R. Mendoza, H.-Y. Chen, J.M. Hiller, D.J. Miller, K. Thornton, P.W. Voorhees, S.B. Adler, S.A. Barnett, Three-dimensional reconstruction of a solid-oxide fuel-cell anode, Nat. Mater. 5 (2006) 541–544, http://dx.doi.org/10.1038/nmat1668.
[22] J.R. Izzo, A.S. Joshi, K.N. Grew, W.K.S. Chiu, A. Tkachuk, S.H. Wang, W.B. Yun, Nondestructive reconstruction and analysis of SOFC anodes using X-ray computed tomography at sub-50 nm resolution, J. Electrochem. Soc. 155 (2008) B504–B508, http://dx.doi.org/10.1149/1.2895067.
[23] P.R. Shearing, J. Golbert, R.J. Chater, N.P. Brandon, 3D reconstruction of SOFC anodes using a focused ion beam lift-out technique, Chem. Eng. Sci. 64 (2009) 3928–3933, http://dx.doi.org/10.1016/j.ces.2009.05.038.
[24] J. Joos, T. Carraro, A. Weber, E. Ivers-Tiffée, Reconstruction of porous electrodes by FIB/SEM for detailed microstructure modeling, J. Power Sources 196 (2011) 7302–7307, http://dx.doi.org/10.1016/j.jpowsour.2010.10.006.
[25] A.P. Cocco, G.J. Nelson, W.M. Harris, A. Nakajo, T.D. Myles, A.M. Kiss, J.J. Lombardo, W.K.S. Chiu, Three-dimensional microstructural imaging methods for energy materials, Phys. Chem. Chem. Phys. 15 (2013) 16377–16407, http://dx.

doi.org/10.1039/c3cp52356j.
[26] B. Tjaden, D.J.L. Brett, P.R. Shearing, Tortuosity in electrochemical devices: a review of calculation approaches, Int. Mater. Rev. 6608 (2016) 1–21, http://dx.doi.org/10.1080/09506608.2016.1249995.
[27] M. Ebner, D.-W. Chung, R.E. García, V. Wood, Tortuosity anisotropy in lithium-ion battery electrodes, Adv. Energy Mater 4 (2014) 1301278, http://dx.doi.org/10.1002/aenm.201301278.
[28] H. Iwai, N. Shikazono, T. Matsui, H. Teshima, M. Kishimoto, Quantification of SOFC anode microstructure based on dual beam FIB-SEM technique, J. Power Sources 195 (2010) 955–961, http://dx.doi.org/10.1016/j.jpowsour.2009.09.005.
[29] P.S. Jørgensen, K. Yakal-Kremski, J. Wilson, J.R. Bowen, S. Barnett, On the accuracy of triple phase boundary lengths calculated from tomographic image data, J. Power Sources 261 (2014) 198–205, http://dx.doi.org/10.1016/j.jpowsour.2014.03.078.
[30] M.E. Lynch, D. Ding, W.M. Harris, J.J. Lombardo, G.J. Nelson, W.K.S. Chiu, M. Liu, Flexible multiphysics simulation of porous electrodes: conformal to 3D reconstructed microstructures, Nanomater. Energy 2 (2013) 105–115, http://dx.doi.org/10.1016/j.nanoen.2012.08.002.
[31] K. Matsuzaki, N. Shikazono, N. Kasagi, Three-dimensional numerical analysis of mixed ionic and electronic conducting cathode reconstructed by focused ion beam scanning electron microscope, J. Power Sources 196 (2011) 3073–3082, http://dx.doi.org/10.1016/j.jpowsour.2010.11.142.
[32] D. Kanno, N. Shikazono, N. Takagi, K. Matsuzaki, N. Kasagi, Evaluation of SOFC anode polarization simulation using three-dimensional microstructures reconstructed by FIB tomography, Electrochim. Acta 56 (2011) 4015–4021, http://dx.doi.org/10.1016/j.electacta.2011.02.010.
[33] Z. Jiao, T. Shimura, N. Shikazono, Numerical assessment of SOFC anode polarization with microstructure evolution, ECS Trans. 68 (2015) 1281–1289, http://dx.doi.org/10.1149/06801.1281ecst.
[34] M. Kishimoto, H. Iwai, M. Saito, H. Yoshida, Three-dimensional simulation of SOFC anode polarization characteristics based on sub-grid scale modeling of microstructure, J. Electrochem. Soc. 159 (2012) B315–B323, http://dx.doi.org/10.1149/2.086203jes.
[35] M. Kishimoto, K. Miyawaki, H. Iwai, M. Saito, H. Yoshida, Effect of composition ratio of Ni-YSZ anode on distribution of effective three-phase boundary and power generation performance, Fuel Cell. 13 (2013) 476–486, http://dx.doi.org/10.1002/fuce.201200174.
[36] K. Miyoshi, H. Iwai, M. Kishimoto, M. Saito, H. Yoshida, Chromium poisoning in (La,Sr)MnO3 cathode: three-dimensional simulation of a solid oxide fuel cell, J. Power Sources 326 (2016) 331–340, http://dx.doi.org/10.1016/j.jpowsour.2016.06.110.
[37] P.R. Shearing, Q. Cai, J.I. Golbert, V. Yufit, C.S. Adjiman, N.P. Brandon, Microstructural analysis of a solid oxide fuel cell anode using focused ion beam techniques coupled with electrochemical simulation, J. Power Sources 195 (2010) 4804–4810, http://dx.doi.org/10.1016/j.jpowsour.2010.02.047.
[38] Q. Cai, C.S. Adjiman, N.P. Brandon, Investigation of the active thickness of solid oxide fuel cell electrodes using a 3D microstructure model, Electrochim. Acta 56 (2011) 10809–10819, http://dx.doi.org/10.1016/j.electacta.2011.06.105.
[39] Q. Cai, C.S. Adjiman, N.P. Brandon, Modelling the 3D microstructure and performance of solid oxide fuel cell electrodes: computational parameters, Electrochim. Acta 56 (2011) 5804–5814, http://dx.doi.org/10.1016/j.electacta.2011.04.065.
[40] B. Rüger, A. Weber, E. Ivers-Tiffee, 3D-modelling and performance evaluation of mixed conducting (MIEC) cathodes, ECS Trans. 7 (2007) 2065–2074, http://dx.doi.org/10.1149/1.2729320.
[41] B. Rüger, J. Joos, A. Weber, T. Carraro, E. Ivers-Tiffée, 3D electrode microstructure reconstruction and modelling, ECS Trans. 25 (2009) 1211–1220, http://dx.doi.org/10.1149/1.3205650.
[42] D.A.W. Gawel, J.G. Pharoah, S.B. Beale, Development of a SOFC performance model to analyze the powder to power performance of electrode microstructures, ECS Trans. 68 (2015) 1979–1987, http://dx.doi.org/10.1149/06801.1979ecst.
[43] T. Carraro, J. Joos, B. Rüger, A. Weber, E. Ivers-Tiffée, 3D finite element model for reconstructed mixed-conducting cathodes: I. Performance quantification, Electrochim. Acta 77 (2012) 315–323, http://dx.doi.org/10.1016/j.electacta.2012.04.109.
[44] T. Carraro, J. Joos, B. Rüger, A. Weber, E. Ivers-Tiffée, 3D finite element model for reconstructed mixed-conducting cathodes: II. Parameter sensitivity analysis, Electrochim. Acta 77 (2012) 309–314, http://dx.doi.org/10.1016/j.electacta.2012.04.163.
[45] K. Miyawaki, M. Kishimoto, H. Iwai, M. Saito, H. Yoshida, Comprehensive understanding of the active thickness in solid oxide fuel cell anodes using experimental, numerical and semi-analytical approach, J. Power Sources 267 (2014) 503–514, http://dx.doi.org/10.1016/j.jpowsour.2014.05.112.
[46] A. Häffelin, J. Joos, M. Ender, A. Weber, E. Ivers-Tiffée, Time-dependent 3D impedance model of mixed-conducting solid oxide fuel cell cathodes, J. Electrochem. Soc. 160 (2013) F867–F876, http://dx.doi.org/10.1149/2.093308jes.
[47] T. Shimura, Z. Jiao, N. Shikazono, Evaluation of nickel-yttria stabilized zirconia anode degradation during discharge operation and redox cycles operation by electrochemical calculation, J. Power Sources 330 (2016) 149–155, http://dx.doi.org/10.1016/j.jpowsour.2016.09.006.
[48] Y.C.K. Chen-Wiegart, R. DeMike, C. Erdonmez, K. Thornton, S.A. Barnett, J. Wang, Tortuosity characterization of 3D microstructure at nano-scale for energy storage and conversion materials, J. Power Sources 249 (2014) 349–356, http://dx.doi.org/10.1016/j.jpowsour.2013.10.026.
[49] A. Nakajo, A.P. Cocco, M.B. DeGostin, A.A. Peracchio, B.N. Cassenti, M. Cantoni, J. Van herle, W.K.S. Chiu, Accessible triple-phase boundary length: a performance metric to account for transport pathways in heterogeneous electrochemical materials, J. Power Sources 325 (2016) 786–800, http://dx.doi.org/10.1016/j.jpowsour.2016.06.046.
[50] M.R. Somalu, V. Yufit, D. Cumming, E. Lorente, N.P. Brandon, Fabrication and characterization of Ni/ScSZ cermet anodes for IT-SOFCs, Int. J. Hydrogen Energy 36 (2011) 5557–5566, http://dx.doi.org/10.1016/j.ijhydene.2011.01.151.
[51] A. Bertei, E. Ruiz-Trejo, F. Tariq, V. Yufit, A. Atkinson, N.P. Brandon, Validation of a physically-based solid oxide fuel cell anode model combining 3D tomography and impedance spectroscopy, Int. J. Hydrogen Energy 41 (2016) 22381–22393, http://dx.doi.org/10.1016/j.ijhydene.2016.09.100.
[52] F. Tariq, M. Kishimoto, V. Yufit, G. Cui, M. Somalu, N.P. Brandon, 3D imaging and quantification of interfaces in SOFC anodes, J. Eur. Ceram. Soc. 34 (2014) 3755–3761, http://dx.doi.org/10.1016/j.jeurceramsoc.2014.05.003.
[53] C.A. Schneider, W.S. Rasband, K.W. Eliceiri, NIH Image to ImageJ: 25 years of image analysis, Nat. Methods 9 (2012) 671–675, http://dx.doi.org/10.1038/nmeth.2089.
[54] C. Kreller, M. Drake, S.B. Adler, H.-Y. Chen, H.-C. Yu, K. Thornton, J.R. Wilson, S.A. Barnett, Modeling SOFC cathodes based on 3-D representations of electrode microstructure, ECS Trans. 35 (2011) 815–822, http://dx.doi.org/10.1149/1.3570062.
[55] A. Bertei, H.W. Choi, J.G. Pharoah, C. Nicolella, Percolating behavior of sintered random packings of spheres, Powder Technol. 231 (2012) 44–53, http://dx.doi.org/10.1016/j.powtec.2012.07.041.
[56] Comsol Inc, Comsol Multiphysics User's Guide, Version 5.2, Burlington, MA, (2016).
[57] H. Zhu, R.J. Kee, Modeling distributed charge-transfer processes in SOFC membrane electrode assemblies, J. Electrochem. Soc. 155 (2008) B715–B729, http://dx.doi.org/10.1149/1.2913152.
[58] A. Bertei, J. Mertens, C. Nicolella, Electrochemical simulation of planar solid oxide fuel cells with detailed microstructural modeling, Electrochim. Acta 146 (2014) 151–163, http://dx.doi.org/10.1016/j.electacta.2014.08.120.
[59] S.J. Cooper, A. Bertei, P.R. Shearing, J.A. Kilner, N.P. Brandon, TauFactor: an open-source application for calculating tortuosity factors from tomographic data, Software 5 (2016) 203–210, http://dx.doi.org/10.1016/j.softx.2016.09.002.
[60] X.H. Liu, Y. Liu, A. Kushima, S. Zhang, T. Zhu, J. Li, J.Y. Huang, In situ TEM experiments of electrochemical lithiation and delithiation of individual nanostructures, Adv. Energy Mater 2 (2012) 722–741, http://dx.doi.org/10.1002/aenm.201200024.
[61] J. Laurencin, R. Quey, G. Delette, H. Suhonen, P. Cloetens, P. Bleuet, Characterisation of Solid Oxide Fuel Cell Ni-8YSZ substrate by synchrotron X-ray nano-tomography: from 3D reconstruction to microstructure quantification, J. Power Sources 198 (2012) 182–189, http://dx.doi.org/10.1016/j.jpowsour.2011.09.105.
[62] J. Deseure, Y. Bultel, L. Dessemond, E. Siebert, Theoretical optimisation of a SOFC composite cathode, Electrochim. Acta 50 (2005) 2037–2046, http://dx.doi.org/10.1016/j.electacta.2004.09.012.
[63] S.C. DeCaluwe, H. Zhu, R.J. Kee, G.S. Jackson, Importance of anode microstructure in modeling solid oxide fuel cells, J. Electrochem. Soc. 155 (2008) B538–B546, http://dx.doi.org/10.1149/1.2898206.
[64] K. Zheng, L. Li, M. Ni, Investigation of the electrochemical active thickness of solid oxide fuel cell anode, Int. J. Hydrogen Energy 39 (2014) 12904–12912, http://dx.doi.org/10.1016/j.ijhydene.2014.06.108.
[65] C.R. Kreller, M.E. Drake, S.B. Adler, Influence of electrode morphology on electrochemical response of SOFC cathodes, ECS Trans. 28 (2010) 105–121, http://dx.doi.org/10.1149/1.3495836.
[66] L. Almar, J. Szász, A. Weber, E. Ivers-Tiffée, Oxygen transport kinetics of mixed ionic-electronic conductors by coupling focused ion beam tomography and electrochemical impedance spectroscopy, J. Electrochem. Soc. 164 (2017) F289–F297, http://dx.doi.org/10.1149/2.0851704jes.
[67] S.S. Nonnenmann, R. Kungas, J. Vohs, D.a Bonnell, Direct in situ probe of electrochemical processes in operating fuel cells, ACS Nano 7 (2013) 6330–6336, http://dx.doi.org/10.1021/nn4023763.
[68] A. Kumar, D. Leonard, S. Jesse, F. Ciucci, E.A. Eliseev, A.N. Morozovska, M.D. Biegalski, H.M. Christen, A. Tselev, E. Mutoro, E.J. Crumlin, D. Morgan, S.H. Yang, A. Borisevich, S.V. Kalinin, Spatially resolved mapping of oxygen reduction/evolution reaction on solid-oxide fuel cell cathodes with sub-10 nm resolution, ACS Nano 7 (2013) 3808–3814, http://dx.doi.org/10.1021/nn303239e.
[69] K.N. Grew, J.R. Izzo, W.K.S. Chiu, Characterization and quantification of electronic and ionic ohmic overpotential and heat generation in a solid oxide fuel cell anode, J. Fuel Cell Sci. Technol. 8 (2011) 31001, http://dx.doi.org/10.1115/1.4002226.
[70] F. Tariq, V. Yufit, X. An, E. Cohen, K. Kareh, A. Bertei, E. Ruiz-Trejo, N.P. Brandon, Tomography - beyond the pretty pictures to numbers for 3D SOFC Electrodes, in: N.P. Brandon (Ed.), 12th Eur. SOFC Forum, Lucerne - Switzerland, 2016, pp. B12045–B12053.
[71] E. Lay-Grindler, J. Laurencin, J. Villanova, P. Cloetens, P. Bleuet, A. Mansuy, J. Mougin, G. Delette, Degradation study by 3D reconstruction of a nickel-yttria stabilized zirconia cathode after high temperature steam electrolysis operation, J. Power Sources 269 (2014) 927–936, http://dx.doi.org/10.1016/j.jpowsour.2014.07.066.
[72] P. Tanasini, M. Cannarozzo, P. Costamagna, A. Faes, J. Van Herle, A. Hessler-Wyser, C. Comninellis, Experimental and theoretical investigation of degradation mechanisms by particle coarsening in SOFC electrodes, Fuel Cell. 9 (2009) 740–752, http://dx.doi.org/10.1002/fuce.200800192.
[73] L. Holzer, B. Iwanschitz, T. Hocker, B. Münch, M. Prestat, D. Wiedenmann, U. Vogt, P. Holtappels, J. Sfeir, A. Mai, T. Graule, Microstructure degradation of cermet anodes for solid oxide fuel cells: quantification of nickel grain growth in dry and in humid atmospheres, J. Power Sources 196 (2011) 1279–1294, http://dx.doi.org/10.1016/j.jpowsour.2010.08.017.
[74] M.H. Pihlatie, A. Kaiser, M. Mogensen, M. Chen, Electrical conductivity of Ni-YSZ

composites: degradation due to Ni particle growth, Solid State Ionics 189 (2011) 82–90, http://dx.doi.org/10.1016/j.ssi.2011.02.001.
[75] M.B. Mogensen, A. Hauch, X. Sun, M. Chen, Y. Tao, S.D. Ebbesen, K.V. Hansen, P.V. Hendriksen, Relation between Ni particle shape change and Ni migration in Ni–YSZ electrodes – a hypothesis, Fuel Cell. 17 (2017) 434–441, http://dx.doi.org/10.1002/fuce.201600222.
[76] D. Kennouche, Y.K. Chen-Wiegart, C. Riscoe, J. Wang, S.A. Barnett, Combined electrochemical and X-ray tomography study of the high temperature evolution of Nickel – yttria Stabilized Zirconia solid oxide fuel cell anodes, J. Power Sources 307 (2016) 604–612, http://dx.doi.org/10.1016/j.jpowsour.2015.12.126.
[77] A. Zekri, K. Herbrig, M. Knipper, J. Parisi, T. Plaggenborg, Nickel depletion and agglomeration in SOFC anodes during long-term operation, Fuel Cell. 17 (2017) 359–366, http://dx.doi.org/10.1002/fuce.201600220.
[78] D. Simwonis, F. Tietz, D. Stover, Nickel coarsening in annealed Ni/8YSZ anode substrates for solid oxide fuel cells, Solid State Ionics 132 (2000) 241–251, http://dx.doi.org/10.1016/S0167-2738(00)00650-0.
[79] G.J. Nelson, K.N. Grew, J.R. Izzo, J.J. Lombardo, W.M. Harris, A. Faes, A. Hessler-Wyser, J. Van Herle, S. Wang, Y.S. Chu, A.V. Virkar, W.K.S. Chiu, Three-dimensional microstructural changes in the Ni-YSZ solid oxide fuel cell anode during operation, Acta Mater. 60 (2012) 3491–3500, http://dx.doi.org/10.1016/j.actamat.2012.02.041.
[80] D. Kennouche, Y.K. Chen-Wiegart, K.J. Yakal-Kremski, J. Wang, J.W. Gibbs, P.W. Voorhees, S.A. Barnett, Observing the microstructural evolution of Ni-Yttria-stabilized zirconia solid oxide fuel cell anodes, Acta Mater. 103 (2016) 204–210, http://dx.doi.org/10.1016/j.actamat.2015.09.055.
[81] P.R. Shearing, R.S. Bradley, J. Gelb, S.N. Lee, A. Atkinson, P.J. Withers, N.P. Brandon, Using synchrotron X-ray nano-CT to characterize SOFC electrode microstructures in three-dimensions at operating temperature, Electrochem. Solid state Lett. 14 (2011) B117–B120, http://dx.doi.org/10.1149/1.3615824.
[82] P.R. Shearing, R.S. Bradley, J. Gelb, F. Tariq, P.J. Withers, N.P. Brandon, Exploring microstructural changes associated with oxidation in Ni-YSZ SOFC electrodes using high resolution X-ray computed tomography, Solid State Ionics 216 (2012) 69–72, http://dx.doi.org/10.1016/j.ssi.2011.10.015.
[83] D.P. Finegan, E. Darcy, M. Keyser, B. Tjaden, T.M.M. Heenan, R. Jervis, J.J. Bailey, R. Malik, N.T. Vo, O.V. Magdysyuk, R. Atwood, M. Drakopoulos, M. DiMichiel, A. Rack, G. Hinds, D.J.L. Brett, P.R. Shearing, Characterising thermal runaway within lithium-ion cells by inducing and monitoring internal short circuits, Energy Environ. Sci. 10 (2017) 1377–1388, http://dx.doi.org/10.1039/C7EE00385D.
[84] R.J. Gorte, S. Park, J.M. Vohs, C. Wang, Anodes for direct oxidation of dry hydrocarbons in a solid-oxide fuel cell, Adv. Mater. 12 (2000) 1465–1469, http://dx.doi.org/10.1002/1521-4095(200010)12:19<1465::AID-ADMA1465>3.0.CO;2–9.
[85] Z. Liu, B. Liu, D. Ding, M. Liu, F. Chen, C. Xia, Fabrication and modification of solid oxide fuel cell anodes via wet impregnation/infiltration technique, J. Power Sources 237 (2013) 243–259, http://dx.doi.org/10.1016/j.jpowsour.2013.03.025.
[86] S.P. Jiang, A review of wet impregnation—an alternative method for the fabrication of high performance and nano-structured electrodes of solid oxide fuel cells, Mater. Sci. Eng. 418 (2006) 199–210, http://dx.doi.org/10.1016/j.msea.2005.11.052.
[87] D. Ding, X. Li, S.Y. Lai, K. Gerdes, M. Liu, Enhancing SOFC cathode performance by surface modification through infiltration, Energy Environ. Sci. 7 (2014) 552, http://dx.doi.org/10.1039/c3ee42926a.
[88] K. Joong Yoon, M. Biswas, H.-J. Kim, M. Park, J. Hong, H. Kim, J.-W. Son, J.-H. Lee, B.-K. Kim, H.-W. Lee, Nano-tailoring of infiltrated catalysts for high-temperature solid oxide regenerative fuel cells, Nanomater. Energy 36 (2017) 9–20, http://dx.doi.org/10.1016/j.nanoen.2017.04.024.
[89] Y. Chen, Y. Zhang, Y. Lin, Z. Yang, D. Su, M. Han, F. Chen, Direct-methane solid oxide fuel cells with hierarchically porous Ni-based anode deposited with nanocatalyst layer, Nanomater. Energy 10 (2014) 1–9, http://dx.doi.org/10.1016/j.nanoen.2014.08.016.
[90] N.M. Farandos, L. Kleiminger, T. Li, A. Hankin, G.H. Kelsall, Three-dimensional inkjet printed solid oxide electrochemical reactors. I. Yttria-stabilized zirconia electrolyte, Electrochim. Acta 213 (2016) 324–331, http://dx.doi.org/10.1016/j.electacta.2016.07.103.
[91] P.C. Su, C.C. Chao, J.H. Shim, R. Fasching, F.B. Prinz, Solid oxide fuel cell with corrugated thin film electrolyte, Nano Lett. 8 (2008) 2289–2292, http://dx.doi.org/10.1021/nl800977z.
[92] S. Kawata, H.-B. Sun, T. Tanaka, K. Takada, Finer features for functional microdevices, Nature 412 (2001) 697–698, http://dx.doi.org/10.1038/35089130.
[93] A. Bertei, F. Tariq, V. Yufit, E. Ruiz-Trejo, N.P. Brandon, Guidelines for the rational design and engineering of 3D manufactured solid oxide fuel cell composite electrodes, J. Electrochem. Soc. 164 (2017) F89–F98, http://dx.doi.org/10.1149/2.0501702jes.